Field emitter activation on cleaned crystalline niobium surfaces relevant for superconducting rf technology

A. Navitski,[1,2,*] S. Lagotzky,[1] D. Reschke,[2] X. Singer,[2] and G. Müller[1]
[1]*University of Wuppertal, FB C Physics Department, 42097 Wuppertal, Germany*
[2]*DESY, 22607 Hamburg, Germany*
(Received 18 January 2013; published 13 November 2013)

The influence of heat treatments at 122, 400, and 800°C on the field emission of large-grain and single-crystal high-purity niobium samples has been investigated. Buffered chemical polishing of 40 μm and high pressure ultrapure water rinsing under clean-room conditions resulted in smooth surfaces with a linear surface roughness of 46 to 337 nm. By means of field emission scanning microscopy, an increasing number of emitters up to 40/cm^2 with temperature were found at surface fields up to 160 MV/m. Two different mechanisms of emitter activation were found, i.e. activation by the applied electric field and activation by temperature. Some emitters with an onset surface field of 50 to 100 MV/m appeared already after the low-temperature bakeout. Correlated scanning-electron-microscopy/energy-dispersive-x-ray measurements revealed particles and surface defects as emitters. Their activation will be discussed with respect to the thickness of the insulating oxide layer.

DOI: 10.1103/PhysRevSTAB.16.112001 PACS numbers: 79.70.+q, 84.71.−b, 74.70.Ad, 81.40.Gh

I. INTRODUCTION

Field emission (FE) is one of the main limitations for the achievable accelerating gradient E_{acc} of superconducting (SC) niobium cavities required for the European x-ray free electron laser (XFEL) [1] and the planned International Linear Collider (ILC) [2] leading to dark currents, x-ray load, radiation activation, power losses, etc. Advanced surface preparation and clean-room techniques for the high-purity Nb cavities for the superconducting radiofrequency (SRF) technology [3] have to be applied to prevent FE at electric surface fields E_{peak} up to 50 MV/m for the XFEL and up to 70 MV/m for the ILC in case of TESLA-type cavities [4] or even up to 85 MV/m if low loss shape [5] of the cavities will be chosen. The main surface preparation steps are chemical etching [6], electropolishing (EP) [7], ethanol rinse [8], and high pressure rinsing (HPR) [9] with ultrapure water to avoid any residues. Two extended surface polishing schemes, i.e. "Final EP" and "BCP Flash" [10], have been chosen for the XFEL production. The first one includes 110 μm EP to remove the surface damage layer and 40 μm final EP and the second one 140 μm EP and 10 μm final buffered chemical polishing (BCP) correspondingly. Two different heat treatments (HTs) are also applied during the fabrication procedure of the actual XFEL cavities. The first one is an annealing at 800°C under high vacuum for some hours after the bulk EP to degas the dissolved hydrogen from the bulk Nb [11] and for stress release. The second one is a final bakeout of the assembled cavities at 120°C for 48 hours just before the cryogenic test to improve the quality factor Q_0 at high gradients [12,13].

Former FE investigations on low- and high-purity Nb samples [14,15] have shown that short ($\sim$ 30 min) HTs at 400 to 800°C create many new emitters at rather low E around 40 MV/m. Beside the activation of some evident particles it was speculated that segregation of impurities at the grain boundaries might contribute to the much enhanced FE. First experiments with a single large-grain (LG) high-purity Nb sample [16], which have been 100 μm BCP etched and 150 bar HPR treated have supported this idea for some emitters but at rather high fields of 250 and 300 MV/m activated by a bakeout at 150°C for 14 hours. Therefore, a systematic investigation of the influence of the different HTs on the FE of SC and LG Nb samples prepared with the actual techniques at DESY has been started.

II. EXPERIMENTAL TECHNIQUES

For the systematic investigation of parasitic FE from the Nb samples a specially constructed field emission scanning microscope (FESM) [17,18] has been used. The FESM (see Fig. 1) is an advanced microscope for the localization and characterization of FE sites on cathodes up to 25 × 25 mm^2 under ultrahigh vacuum (10^{-7} Pa) conditions. At first, each sample surface was tilt corrected with respect to a truncated cone anode of 300 μm in diameter to achieve a constant gap Δz and correspondingly constant electric field E within around ±10% over the

*Corresponding author.
aliaksandr.navitski@desy.de

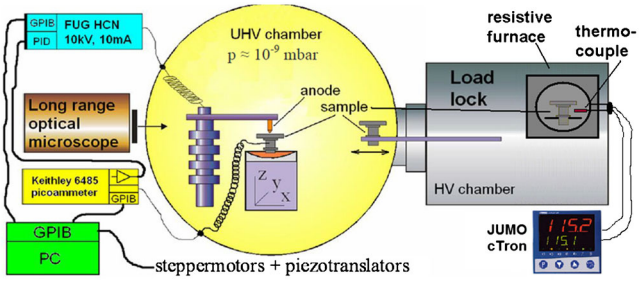

FIG. 1. Schematic view of the FESM.

maximum scan area. Then all emitters which are active below a certain chosen maximum field were nondestructively localized by means of voltage scans $V(x, y)$ at $\Delta z = 50\ \mu$m while keeping the FE current below the threshold of typically 1 nA. The procedure applies a proportional-integral-derivative (PID)-regulated power supply (FUG HCN100M) providing up to 10 kV voltage (correspond to around 200 MV/m at $\Delta z = 50\ \mu$m) and an analog electrometer (Keithley 610 C). Emitter distribution maps with 67×67 points for 1 cm^2 area were obtained at macroscopic dc electric fields $E_{\text{scan}} = V(x, y)/\Delta z$ typically between 100 and 160 MV/m in steps of 20 MV/m. The local FE measurements of some selected emitters were performed giving the values of the onset field E_{on} (defined as a macroscopic electric field required for 1 nA FE current), effective field enhancement factor β, and emission area S. It gives also the overall behavior of the $I - V(I - E)$ characteristics of the found FE sites. The macroscopic electric field E was calibrated for each emitter as the linear slope of the PID-regulated $V(z)$ dependence for fixed FE current of 1 nA by displacing the sample (cathode) position z with respect to the fixed anode. The real distance d between the anode and a relevant emitter was determined by the linear extrapolation of the $V(z)$ curve to zero voltage. The local $I - V(I - E)$ measurements were performed using a digital pico-ammeter (Keithley 6485) with a protection circuit as described elsewhere [19]. All data were taken and recorded by a LABVIEW®-based software.

For the heat treatment (HT) experiments on the Nb samples a resistive furnace has been recently installed into the load-lock chamber of the FESM. The *in situ* furnace provides temperatures up to 1200°C under high vacuum conditions ($< 10^{-4}$ Pa). All the inner parts of the furnace were degreased with acetone, blown clean with ionized nitrogen, and baked several times up to at least

TABLE I. Overview of the heat treatments.

	Temperature, °C	Duration, *h*	Warm-up, °C/ min
HT122	122	24	~0.54 (3 h)
HT400	400	2	~6.25 (1 h)
HT800	800	2	~12.91 (1 h)

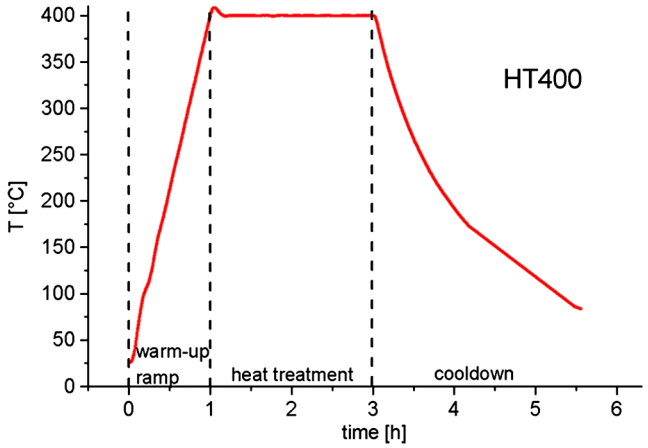

FIG. 2. Temperature profile for the heat treatment at 400°C.

900°C for half an hour. The temperature inside the furnace was measured with a thermocouple (Pt10Rh-Pt) and controlled by a commercial PID controller (JUMO cTRON 04). Three HTs up to 122, 400, and 800°C and of different duration were sequentially applied to the Nb samples and alternated with the FESM measurements. The main parameters of the heating cycles are similar to those used during the Nb cavity fabrication process (HT122, HT800) [10] or to former FE studies (HT400, HT800) [14,15] and listed in Table I. A typical temperature profile with linear warm-up ramp, HT at the nominal temperature (± 1°C) over a given duration and natural cool-down is shown in Fig. 2. All the sequences of the HT and FESM study of the samples have been performed without breaking the vacuum.

The surface quality of the fabricated Nb samples was examined before the final BCP of 10 μm and HPR (see Sec. III) by means of a profilometer setup [20] consisting of an optical profilometer (OP) and an atomic force microscope (AFM, ±2 μm positioning accuracy with respect to the OP), and a CCD camera. The setup is installed on a massive granite plate with a passive vibration damping system. Guided by the CCD camera for fast positioning of the sample, the chromatic aberration sensor of the OP provides a lateral (vertical) resolution of 2 μm (3 nm) on samples up to 20×20 cm^2. Further zooming into defect areas of $95 \times 95\ \mu$m^2 down to the lateral nm range is possible with the AFM in contact or noncontact modes. A horizontal laminar air flow from the back (class ISO 5) ensures clean-room-like measurement conditions. An external scanning electron microscopy (SEM) with energy dispersive x-ray analysis (EDX) was used for the final inspection of the sample surface and foreign material inclusions in the localized emitter regions.

III. SAMPLE PREPARATION AND SURFACE QUALITY CONTROL

Four flat samples with a diameter of 26.5 mm were cut from high-purity (RRR > 250) SC or LG Nb sheets and

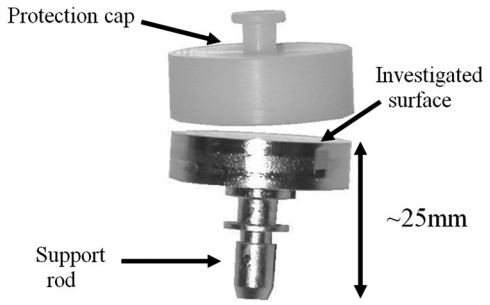

FIG. 3. Nb sample with Teflon® protection cap.

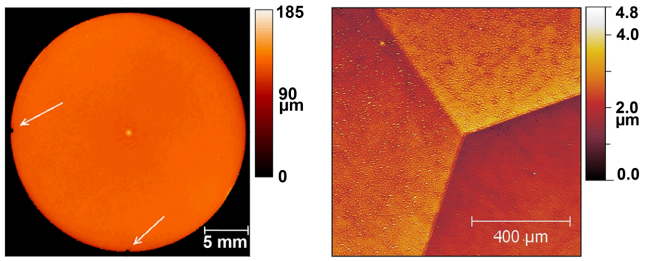

FIG. 4. Full optical profilometry map of a SC Nb sample (left) with ~30 μm lateral resolution showing the two marks (white arrows) and higher resolution (~ 2 μm) map of a LG sample (right).

electron beam welded to support rods (Fig. 3). Such samples can be assembled in the main coupler port of nine-cell XFEL cavities during the chemical treatments [21]. Two marks on the circumference of the samples serve for the identification of their angular position in different measurement systems (see Fig. 4, left). Both LG samples contain three large grains with the grain boundary junction in the middle of the sample (see Fig. 4, right). BCP using $HF(40\%)/HNO_3(65\%)/H_3PO_4(85\%)$ in volume ratio 1:1:2 of all samples have been done in two steps: first a layer of about 30 μm was removed for the OP/AFM surface quality control and then again 10 μm to refresh the sample surface before the final HPR cleaning with ultrapure water under clean-room conditions at DESY. The transport of the samples between all the various measurements was performed under Teflon® protection caps (see Fig. 3) and sealed in plastic bags to avoid pollution as much as possible. The protection caps were removed in the OP/AFM under laminar air flow and in the FESM under high vacuum conditions.

At first the OP was used to determine the surface flatness of the samples within the area of ~1 cm^2 envisaged for the FESM scans. For all samples the overall flatness stayed within ± 2 μm, i.e. the resulting field inhomogeneity ($\pm$ 4%) is in the same order of magnitude as that due to the finite tilt correction (see Sec. II). The base linear roughness R_a of the fabricated Nb samples after 30 μm BCP was determined by the OP measurements (Fig. 4) in defect-free regions of 1×1 mm^2 size. The LG samples showed different R_a values (148 to 337 nm, as measured within the grains) which were higher than those of the SC samples (46 to 80 nm). Few local defects up to some 10 μm height were also found on the OP maps, and their morphology suggested both particulates and scratch nature. In order to estimate the maximum electric field enhancement factor β_{max} which might locally occur for such surfaces, more accurate profilometry measurements of the Nb surface with AFM were performed as shown in Fig. 5. Obviously, there are many ridgelike and tiplike protrusions with height h and curvature radius r which can be directly measured with the AFM. A good approximation of the electric field enhancement in an extended field is $\beta \approx h/r$ [22]. Accordingly, typical β_{max} values of 7–15 (left), 8–12 (middle), and 3.5–6 (right image) were derived from selected AFM profilometry maps in Fig. 5. High β_{max} values (> 10) might also result for large and rough particles (> 2 μm), while small grain boundaries steps (< 2 μm) should not be crucial for FE ($\beta_{max} < 4$) [23,24]. For Nb with a typical work function φ of 4 eV [25], Fowler-Nordheim-like FE of 1 $nA/\mu m^2$ should start at $2000/\beta_{max}$ MV/m [26].

IV. FE RESULTS AND DISCUSSION

The sequential FESM-HT-FESM investigations led to the expected activation of emitters with temperature. In Fig. 6 the maps of emitters found at $E_{scan} = 160$ MV/m on a LG Nb sample after the different treatments are shown. Obviously the emitter number density N increased slightly after HT122 but strongly after higher temperature HTs. Most emitters occur rather on the grains than on the grain boundaries, i.e. in contrast to a previous LG sample after

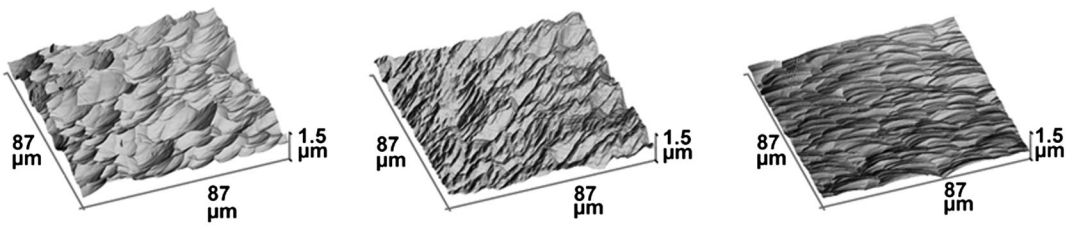

FIG. 5. AFM image of the three different grains shown in Fig. 4 (right) with roughness of 313, 298, and 152 nm from left to right correspondingly.

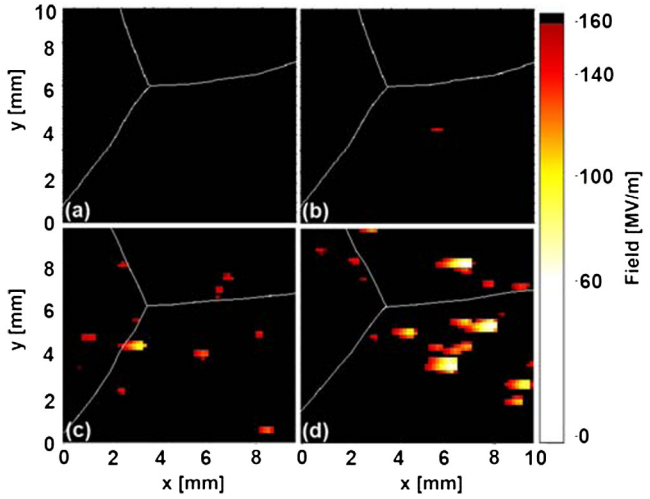

FIG. 6. Distribution maps of emitters with E_{on} (at 1 nA) up to 160 MV/m of a LG Nb sample in the same area with no HT (a), after HT122 (b), HT400 (c), and HT800 (d). The lines mark the position of the grain boundaries.

100 μm BCP [16]. Therefore, the speculation of a grain boundary assisted FE cannot be confirmed in the actual study at least up to fields of 160 MV/m. There is, however, some evidence that N depends on the grain orientation due to the different roughness, but the statistical error is still too large to prove this consideration. On the other side there is an activation of emitters due to the applied electric field, too. Therefore, the emitters can be activated either by electric field or by temperature. Finally, the emitters appear at lower onset field as compared to the initially applied field. Therefore, it is necessary to distinguish between the initial activation field E_{act} which is in our case equal to the maximum field applied during the voltage scans E_{scan} and the final onset field E_{on}. It is helpful also to define the field reduction factor $\rho = E_{act}/E_{on}$. All emitters appeared finally at the onset field $E_{on} < E_{act}$ with a maximum $\rho \approx 1.7$ for the strong emitters on this LG Nb sample.

Similar maps were obtained for the other LG and both SC Nb samples at the same field steps. The number of emitters activated by the HTs on each type of sample has been investigated to get the scaling of N with the activation field E_{act} as shown in Fig. 7. While the slope of N vs E_{act} curves seems to be linear for HT800 data, it looks rather exponential for the other HT cases, especially for the HT400 one. Such an exponential increase of N with field was already observed for electropolished polycrystalline

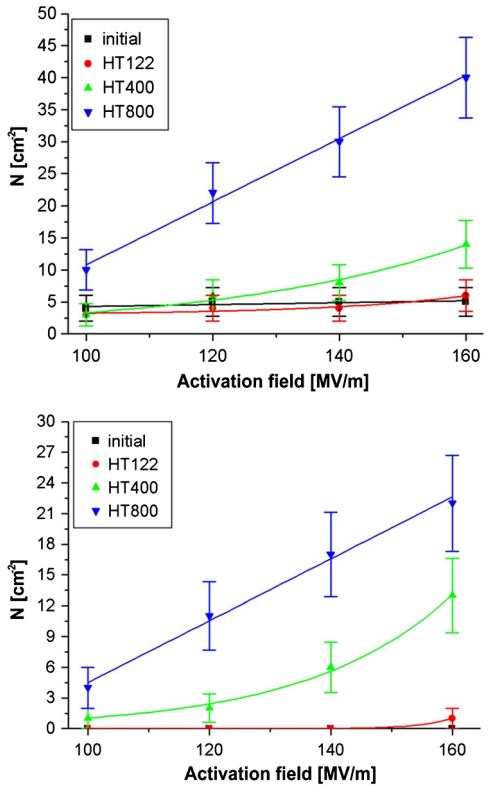

FIG. 7. Emitter number density on the SC (upper) and LG (lower, please note the different scales) Nb samples at various activation fields E_{act} before and after the HTs.

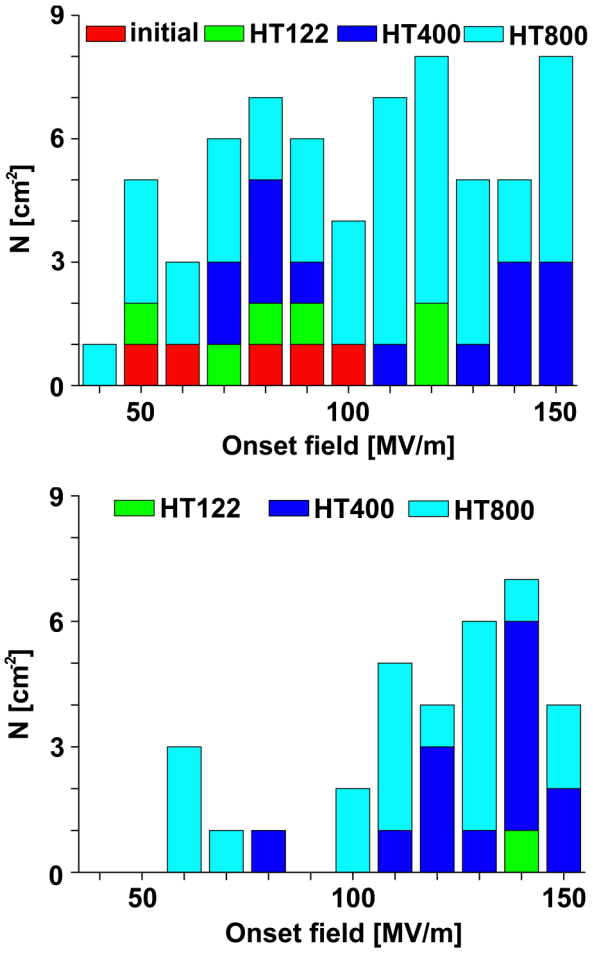

FIG. 8. Stacked histogram of the emitter number density at E_{on} (at 1 nA) after each HT on SC (top) and LG (bottom) Nb samples.

Nb samples without any HT [24]. The modification of the $N(E_{act})$ slope to the linear increase seems to be induced by the HTs. Two different mechanisms for emitter activation must be considered here, i.e. activation by the applied electric field and activation by temperature. Figure 8 shows that most emitters activated by field or low-temperature HT122 result already in rather low E_{on} between 50 and 100 MV/m, what would be crucial for accelerators like XFEL and ILC.

In order to analyze the underlying FE mechanism, local $I(E)$ measurements of 15 strong emitters from the maps have been performed. The resulting $I(E)$ curves were fitted to the modified Fowler-Nordheim (FN) law [26]:

$$I_{FN} = A\frac{SE^2\beta^2}{\varphi t^2(y)}\exp\left(-B\frac{\varphi^{3/2}v(y)}{E\beta}\right),$$

where β is effective local electric field enhancement of the emitter and S is fit parameter interpreted as emission area. For S in m^2, φ in eV, and E in V/μm, the constants are $A = 154$ and $B = 6830$. The image charge correction functions t and v were set to 1 for simplicity. Typical examples of FN-like $I(E)$ curves are given in Fig. 9. The

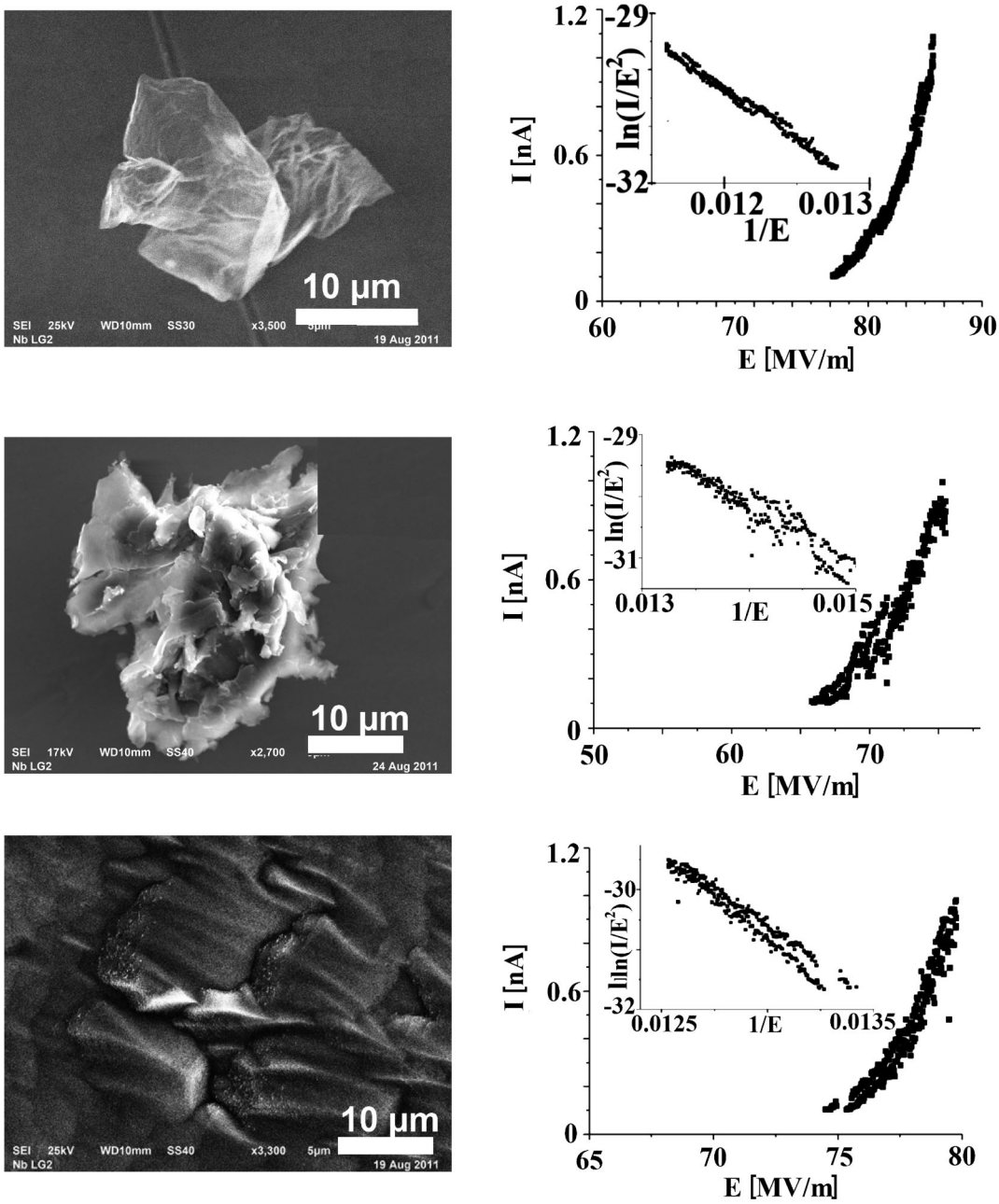

FIG. 9. SEM images (left) and $I - E$ curves (right) with FN plots (insets) of HT-activated emitters: Nb particle (top), Al particle (middle), and surface irregularity (bottom).

resulting β values of the activated emitters were between 14 and 85, i.e. significantly higher than the ones estimated from the OP and AFM measurements. This difference hints for the presence of particles with complex shape, i.e. sharper emitter features than resolvable with our profilometry. It is remarkable that the resulting S values of the activated emitters were in the range of 0.001 to 1000 μm^2 which is still reasonable with respect to the typical size of residual particles and surface defects.

In order to identify the activated emitters, the dominant emitting regions in all final FE maps (around 30) were investigated by means of SEM with EDX analysis. The emission sites were mostly ($\sim 67\%$) related to particles of about 2 to 20 μm size, and the others showed various kinds of surface irregularities. The EDX analysis revealed foreign material inclusions (e.g. Al or Si) only for some of the particles. The SEM images of three FN-like emitters are presented in Fig. 9. While the flakelike Nb particle might stem from the *in situ* furnace, the rough Al particle looks more like a residue of the BCP/HPR. The origin of the surface irregularity is less clear, yet. In any case the FE results show that such surface defects or inclusions can be activated as emitters by heat treatments. The emitter activation by the electric field explains also one of the drawbacks of the high power processing of SC Nb cavities [27] which aimed an elimination of the FE load and lead to surface damages and permanent emitter activation.

The most likely explanation for the observed emitter activation by the applied electric field is the metal-insulator-metal (MIM) model for conducting particles and the metal-insulator-vacuum (MIV) model for surface irregularities, both proposed by Latham *et al.* [28]. The emitters become activated as soon as the surface field is high enough to burn a conduction channel through the insulating oxide layer which is naturally present on the Nb surface and is typically between 2 and 5 nm [29]. Measurements have shown that E_{act} of a surface defect is directly proportional to the thickness d_{Ox} of the Nb_2O_5 layer [30]. The final onset field E_{on} of an activated emitter is then determined by the geometry of the defect. The role of the surface oxide layer for the FE activation has been partially confirmed by some preliminary experiments on the FE studies after oxide layer recovery. Some deactivation or weakening of the FE has been observed after an exposure of the Nb sample to ambient air for some hours under the protection caps. More detailed experiments including HPR cleaning after HT should follow.

The competition of the two different activation mechanisms becomes more clear in Fig. 10, where the ρ values as well as the ratio of emitters activated by field N^E_{act} and by temperature N^T_{act} to the total number of emitters N are separately given for the HTs. With increasing temperature, the range as well as the mean ρ values becomes smaller. For polycrystalline Nb samples without any HT, higher ρ values of 2 to 4 were observed [24]. This reduction of ρ by HTs

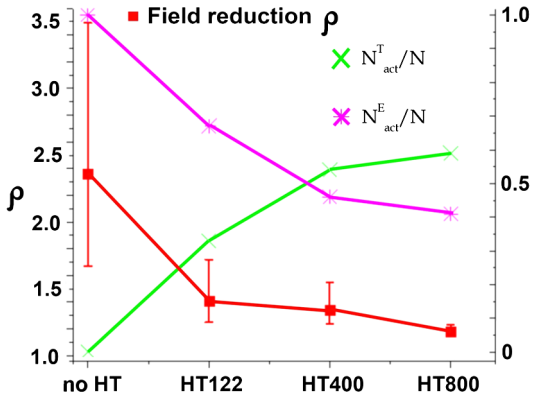

FIG. 10. Field reduction factor ρ (left scale) and ratio of field-(N^E_{act}/N) and HT-(N^T_{act}/N) activated emitters (right scale) on a LG Nb sample.

should be related to the decreasing of thickness d_{Ox} of the natural insulating oxide layer which was confirmed by XPS measurements on annealed Nb cavities [31]. It is well known that already at moderate temperatures the oxygen diffusion into the bulk Nb [11] and the oxygen desorption as CO or CO_2 [32] due to contamination layer lead to a conversion of the insulating Nb_2O_5 layer into semiconducting NbO_2 and conducting NbO layers. Finally, the insulating layer is completely removed after HTs above around 500°C [32]. This explains also the saturation trend of the $N^T{}_{\mathrm{act}}$ curve vs temperature of the HTs above 400°C. The remaining number of emitters activated by the field even after the HTs at 800°C is explained most probably by thicker oxide layers in the defect regions and/or due to presence of insulating particulates on the surface which requires much higher fields for burning of the conducting channels. For increasing temperature, therefore, more emitters become activated by the HT and less by the field. These considerations are also confirmed by the observation that N decreases with increasing oxide layer thickness [30].

A quantitative check of the effect of the different HTs on the emitters is possible when the oxide layer thickness is taken into account. In Fig. 11 the total N of HT-activated

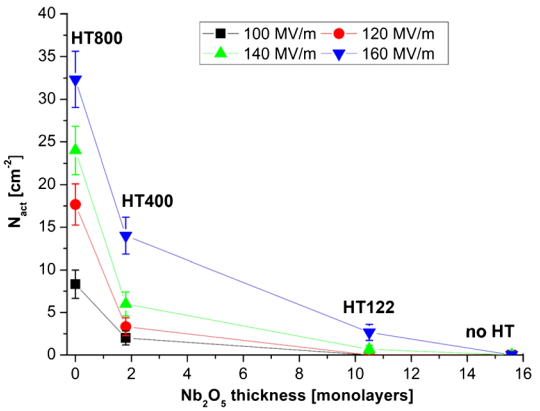

FIG. 11. Emitter number density at different electric field versus thickness of Nb_2O_5 (as derived from [32]).

emitters obtained at the different E_{act} is plotted as a function of the oxide layer thickness. The first emission appears at rather high fields (i.e. 160 MV/m) after slight reduction of the oxide thickness after HT at 122°C. With decreasing d_{Ox}, N increases even for lower electric fields. Slightly different diffusion lengths and oxygen desorption rate for different crystal orientation might also contribute to the varying number of activated emitters in the three areas of the LG Nb samples (Fig. 6).

One could expect additional enhancement of the FE due to lowering of the work function of the surface especially in the defect areas due to carbon contaminants, e.g. a monolayer-thick NbC formed on the surface upon cool-down from around 500°C to room temperature and, subsequently, with the growth of a graphite layer due to contamination by residual gas [32]. However, the carbon concentration at room temperature is almost the same or even less after the heating cycle. It means the carbon contaminants should have most probably no effect on the emitter activation. Segregation of such impurities in some defect areas like in Fig. 9, bottom, might lead, however, to new emitters. Detailed investigations of such defect areas and particulates including composition evolution would be essential for the full understanding of the emitter activation process. This is, however, a very difficult experimental task and could not be realized within the actual work.

Measurements of the work function of Nb with respect to different crystal orientations and heat treatments might be performed by applying intrinsic FE measurements as it was done previously [16]. However, it is not applicable for the actual studies as the method requires a superior quality of Nb samples and can be performed only on absolutely clean and defect-free Nb. The work function measurements with this method have resulted in a relatively big absolute measurement error of at least 17% to 27%, too.

It would be also interesting to investigate the activation effect by further increase of the temperature of the HTs. If the activation process is driven only by the niobium oxide thickness, one should expect a saturation or decrease of the emitter activation at temperatures above 800°C.

It was a common practice in the early days of SRF cavities to anodize the inner surface to grow an oxide layer with a thickness in the range of 0.1 μm [33,34]. It was found that the anodic oxide film not only proved suitable as a protective film, but also produced a considerable increase in the quality factor and the critical magnetic field. It was observed also that instabilities, caused mostly by FE effects and occurring occasionally upon increase the rf field, are totally eliminated by the oxide film. The oxide layer plays a crucial role for the FE as suggested by the actual studies as well and, therefore, it should be considered to apply the anodization to the actual SC cavities to mitigate FE and allow further studies.

V. CONCLUSIONS AND OUTLOOK

It was shown that FE from particles and defects on cleaned crystalline Nb surfaces relevant for SRF technology can be activated not only by high electric field but also by HTs which are usually applied to Nb cavities. A strong increase of the emitter number density with temperature has been observed which starts already after the rather moderate final bakeout of the assembled cavities and might be crucial for the achievable E_{acc} especially of the planned ILC. The ratio of emitters activated by HTs increases with temperature and seems to saturate at a certain level, whereas the ratio of emitters activated by electric field and the field reduction factor decreases. Moreover, the increase of N with the activation field stays exponential after HTs up to 400°C but becomes linear after HT at 800°C. Enhanced FE at grain boundaries with steps of a few μm has not been observed up to 160 MV/m. These observations support the MIM and MIV model as initial FE mechanism of particles and surface defects, respectively. Both depend strongly on the thickness of Nb surface oxide, which disappears with temperature due to the increase of oxygen diffusion into Nb and oxygen desorption.

More systematic FE investigations on Nb samples after HTs at 120–400°C combined with intermediate SEM studies are foreseen for more detailed understanding of the FE and activation mechanisms of particles and surface defects. Coating of the surface of the actual superconducting cavities with a thicker dielectric layer should also be considered for suppression of their parasitic FE load as long as the resulting quality factor and quench field are not affected.

ACKNOWLEDGMENTS

We thank R. Heiderhoff for access to the high resolution SEM with EDX at FB E of University of Wuppertal and J. Ziegler for the help with HPR treatments at DESY. This work was funded in part by the Helmholtz-Allianz "Physics at the Terascale" and BMBF Project No. O5H09PX5.

[1] Report No. DESY 2006-097, 2007 [http://www.xfel.eu/dokumente/technical_documents].
[2] http://www.linearcollider.org.
[3] H. Padamsee, *RF Superconductivity* (Wiley-VCH, New York, 2009).
[4] E. Haebel, A. Mosnier, and J. Sekutowicz, in Proceedings of the XVth International Conference on High Energy Accelerators, Hamburg, Germany, 1992, Vol. 2, pp. 957–959.
[5] J. Sekutowicz, K. Ko, L. Ge, L. Lee, Z. Li, C. Ng, G. Schussman, L. Xiao, I. Gonin, T. Khabibouline, N. Solyak, Y. Morozumi, K. Saito, and P. Kneisel, in *Proceedings of the 21st Particle Accelerator Conference, Knoxville, 2005* (IEEE, Piscataway, NJ, 2005), p. 3342, TPPT056.

[6] L. Lilje, C. Antoine, C. Benvenuti, D. Bloess, J.-P. Charrier, E. Chiaveri, L. Ferreira, R. Losito, A. Matheisen, H. Preis, D. Proch, D. Reschke, H. Safa, P. Schmüser, D. Trines, B. Visentin, and H. Wenninger, Nucl. Instrum. Methods Phys. Res., Sect. A **516**, 213 (2004).

[7] H. Diepers, O. Schmidt, H. Martens, and F. S. Sun, Phys. Lett. A **37**, 139 (1971).

[8] B. van der Horst, A. Matheisen, B. Petersen, S. Saegebarth, and P. Schilling, in Proceedings of the 13th Workshop on RF Superconductivity, Beijing (2007), TUP30.

[9] P. Kneisel and B. Lewis, in Proceedings of the 7th Workshop on RF Superconductivity, Gif sur Yvette (1995), p. 31.

[10] D. Reschke *et al.*, Phys. Rev. ST Accel. Beams **13**, 071001 (2010).

[11] E. Fromm and E. Gebhardt, *Gase und Kohlenstoff in Metallen* (Springer-Verlag, Berlin, 1976).

[12] B. Visentin, J. P. Charrier, B. Coadou, and D. Roudier, in *Proceedings of the International Workshop on Radiofrequency Superconductivity* (Los Alamos National Laboratory, Santa Fe, NM, 1999), p. 198, and references therein.

[13] G. Ciovati, Appl. Phys. Lett. **89**, 022507 (2006).

[14] P. Niedermann, N. Sankarraman, R. J. Noer, and O. Fischer, J. Appl. Phys. **59**, 892 (1986).

[15] E. Mahner, in *Proceedings of the 6th Workshop on RF Superconductivity, Newport News, 1993*, p. 252 [Part. Accel. 46, 67 (1994)].

[16] A. Dangwal, G. Müller, D. Reschke, and X. Singer, Phys. Rev. ST Accel. Beams **12**, 023501 (2009).

[17] E. Mahner, N. Minatti, H. Piel, and N. Pupeter, Appl. Surf. Sci. **67**, 23 (1993).

[18] D. Lysenkov and G. Müller, Int. J. Nanotechnology **2**, 239 (2005).

[19] A. Navitski, G. Müller, V. Sakharuk, T. W. Cornelius, C. Trautmann, and S. Karim, Eur. Phys. J. Appl. Phys. **48**, 30502 (2009).

[20] http://www.frt-gmbh.com/en.

[21] G. Müller, A. Göhl, T. Habermann, A. Matheisen, D. Nau, D. Proch, and D. Reschke, in *Proceedings of the 6th European Particle Accelerator Conference, Stockholm, 1998* (IOP, London, 1998), p. 1876.

[22] T. Utsumi, IEEE Trans. Electron Devices **38**, 2276 (1991).

[23] A. Navitski, S. Lagotzky, G. Müller, D. Reschke, and X. Singer, *Proceedings of the 14th International Conference on RF Superconductivity* (Institute of Physics Publishing, Bristol and Philadelphia, 2009), p. 316.

[24] A. Navitski, Ph.D. dissertation, University of Wuppertal, 2010.

[25] CRC Handbook of Chemistry and Physics, 87th edition (2006).

[26] R. G. Forbes, J. Vac. Sci. Technol. B **17**, 526 (1999).

[27] J. Kirchgessner, P. Barnes, L. Bartelsons, M. Champion, C. Crawford, H. Edwards, J. Graber, K. Koepket, M. Kuchnirt, A. Matheisen, D. Metzger, D. Moffat, H. Muller, H. Padamsee, M. Pekeler, H. Pfeffert, P. Schmüser, J. Sears, and M. Tigner, in *Proceedings of the Particle Accelerator Conference, Washington, DC, 1993* (IEEE, New York, 1993), p. 918.

[28] R. V. Latham, Vacuum **32**, 137 (1982).

[29] M. Grundner and J. Halbritter, J. Appl. Phys. **51**, 397 (1980).

[30] A. T. Wu, S. Jin, X. Y. Lu, R. A. Rimmer, and K. Zhao, in *Proceedings of the 2nd International Particle Accelerator Conference, San Sebastián, Spain* (EPS-AG, Spain, 2011), p. 355.

[31] T. Proslier, J. Zasadzinski, J. Moore, M. Pellin, J. Elam, L. Cooley, C. Antoine, J. Norem, and K. E. Gray, Appl. Phys. Lett. **93**, 192504 (2008).

[32] A. Dacca, G. Gemme, L. Mattera, R. Parodi, Appl. Surf. Sci. **126**, 219 (1998).

[33] H. Pfister, Cryogenics **16**, 17 (1976).

[34] H. Martens, H. Diepers, and R. K. Sun, Phys. Lett. A **34**, 439 (1971).